Inorganic Chemistry

Article

pubs.acs.org/IC

Hyperfine Coupling Constants on Inner-Sphere Water Molecules of a Triazacyclononane-based Mn(II) Complex and Related Systems Relevant as MRI Contrast Agents

Véronique Patinec,[§] Gabriele A. Rolla,[‡] Mauro Botta,[‡] Raphaël Tripier,[§] David Esteban-Gómez,[†] and Carlos Platas-Iglesias*[,†]

[†]Departamento de Química Fundamental, Facultade de Ciencias, Universidade da Coruña, Campus da Zapateira-Rúa da Fraga 10, 15008 A Coruña, Spain

[‡]Dipartimento di Scienze e Innovazione Tecnologica, Università del Piemonte Orientale "Amedeo Avogadro", Viale T. Michel 11, 15121 Alessandria, Italy

[§]Université de Bretagne Occidentale, UMR-CNRS 6521, UFR des Sciences et Techniques, 6 avenue Victor le Gorgeu, C.S. 93837, 29238 BREST Cedex 3, France

Supporting Information

ABSTRACT: We report the synthesis of the ligand H_2MeNO2A (1,4-bis(carboxymethyl)-7-methyl-1,4,7-triazacyclononane) and a detailed experimental and computational study of the hyperfine coupling constants (HFCCs) on the inner-sphere water molecules of [Mn(MeNO2A)] and related Mn^{2+} complexes relevant as potential contrast agents in magnetic resonance imaging (MRI). Nuclear magnetic relaxation dispersion (NMRD) profiles, ^{17}O NMR chemical shifts, and transverse relaxation rates of aqueous solutions of [Mn(MeNO2A)] were recorded to determine the parameters governing the relaxivity in this complex and the ^{17}O and ^{1}H HFCCs. DFT calculations (TPSSh model) performed in aqueous solution (PCM model) on the $[Mn(MeNO2A)(H_2O)]\cdot xH_2O$ and $[Mn(EDTA)(H_2O)]^{2-}\cdot xH_2O$ (x = 0−4) systems were used to determine theoretically the ^{17}O and ^{1}H HFCCs responsible for the ^{17}O NMR chemical shifts and the scalar contributions to ^{17}O and ^{1}H NMR relaxation rates. The use of a mixed cluster/continuum approach with the explicit inclusion of a few second-sphere water molecules is critical for an accurate calculation of HFCCs of coordinated water molecules. The impact of complex dynamics on the calculated HFCCs was evaluated with the use of molecular dynamics simulations within the atom-centered density matrix propagation (ADMP) approach. The ^{17}O and ^{1}H HFCCs calculated for these complexes and related systems show an excellent agreement with the experimental data. Both the ^{1}H and ^{17}O HFCCs (A_{iso} values) are dominated by the spin delocalization mechanism. The A_{iso} values are significantly affected by the distance between the oxygen atom of the coordinated water molecule and the Mn^{2+} ion, as well as by the orientation of the water molecule plane with respect to the Mn−O vector.

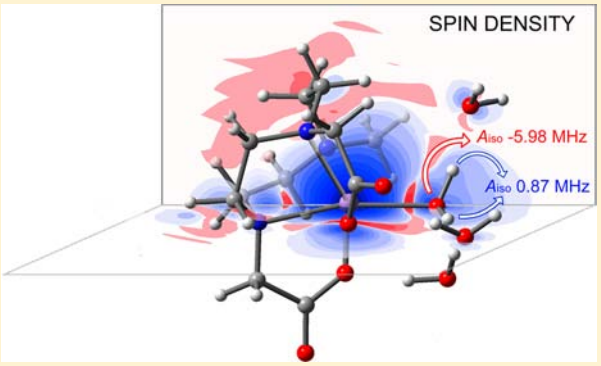

INTRODUCTION

Magnetic resonance imaging (MRI) is a diagnosis technique widely used in radiology to obtain detailed images of the body. MRI uses the NMR signal of water protons present in the body, and the contrast between different tissues is related to their intrinsic proton densities and longitudinal ($1/T_1$) and transverse ($1/T_2$) proton relaxation rates.[1] It soon became obvious that certain paramagnetic species, the so-called contrast agents (CAs), could be used to increase the contrast between the specific tissue or organ of interest and the surrounding tissues of the body. CAs possess the ability to enhance proton relaxation rates in the tissue in which they are distributed, therefore increasing image contrast. Most of the compounds that entered into clinical practice as CAs are Gd^{3+} complexes with poly(aminocarboxylate) ligands ensuring a high thermodynamic stability to prevent the release of the toxic free Gd^{3+} ion.[2] Gd^{3+} was selected for this purpose because it is one of the most paramagnetic ions and presents a slow electronic relaxation thanks to its isotropic $4f^7$ electronic configuration. CAs based on Gd^{3+} chelates must contain at least one water molecule coordinated to the metal ion that exchanges rapidly with the bulk water.

Complexes of the d^5 metal ion Mn^{2+} with high-spin configuration represent an alternative to the classical Gd^{3+}-based contrast agents.[3] Such Mn^{2+} complexes present relatively high effective magnetic moments, slow electronic relaxation rates, and relatively fast exchange rates of inner-sphere water molecules, thereby imparting an efficient mechanism for the longitudinal and transverse relaxation enhancement of bulk

Received: June 6, 2013
Published: September 26, 2013

   dx.doi.org/10.1021/ic4014366 | Inorg. Chem. 2013, 52, 11173−11184

water protons. Indeed, the water exchange rate determined for $[Mn(H_2O)_6]^{2+}$ ($\sim 4 \times 10^6$ s^{-1}) is considerably faster than that observed for the trivalent d^5 analogue $[Fe(H_2O)_6]^{3+}$ ($\sim 2 \times 10^2$ s^{-1}),[4] and a similar situation is observed, for instance, for the corresponding EDTA complexes.[5] The efficiency of a paramagnetic complex as a CA is estimated by its proton relaxivity, r_{1p}, which refers to the relaxation enhancement of water protons promoted by a 1 mM concentration of the paramagnetic metal ion. An important potential advantage of Mn^{2+}-based CAs over the classical Gd^{3+}-based ones is the lower toxicity of Mn^{2+} compared with the Gd^{3+}. Indeed, the issue of Gd^{3+} toxicity is receiving increasing attention due to the recent discovery of a disease (nephrogenic systemic fibrosis) related to the administration of Gd^{3+}-based contrast agents to patients affected by renal impairment.[6]

In contrast to the plethora of small Gd^{3+} complexes investigated as potential MRI CAs in the last 25 years,[2] the number of Mn^{2+} chelates investigated for that purpose is relatively small. Among the different Mn^{2+} complexes investigated so far are $[Mn(EDTA)(H_2O)]^{2-}$ and EDTA derivatives,[7,8] complexes with tetraaza macrocycles containing carboxylate or methylenephosphonate pendant arms (1,4-H_2DO2A, HDO1A, H_2L1, and HL2, Chart 1),[9,10] 1-oxa-4,7-diazacyclononane and triazacyclononane derivatives containing acetic, phosphonic, or phosphinic acid pendant arms,[11−13] hexadentate macrocyclic ligands based on the 6-amino-6-methylperhidro-1,4-diazapine scaffold,[14] and pentadentate macrocyclic ligands (i.e., L3, Chart 1).[15]

Chart 1

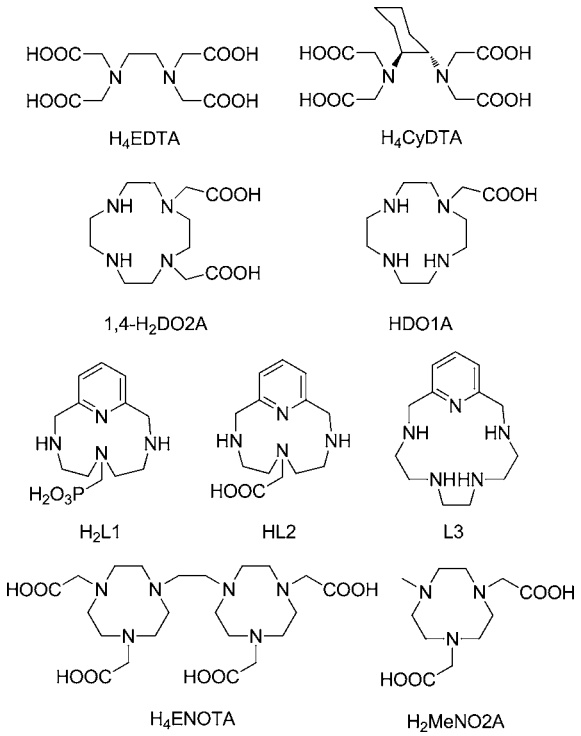

The relaxivity of a Mn^{2+}-based CA is accounted for by the presence of two different contributions: outer-sphere relaxation, which is the result of free diffusion of water molecules in the vicinity of the metal center, and inner-sphere relaxation, which arises from the exchange between the coordinated water molecule(s) and the bulk water. The inner-sphere contribution is proportional to the number of water molecules coordinated to the metal ion (q). The ^{1}H longitudinal relaxation rate of the inner-sphere water molecules is dominated by the dipolar interaction, which is proportional to $1/r_{MnH}^6$, where r_{MnH} is the distance between Mn^{2+} and the inner-sphere water proton nuclei. Furthermore, the inner-sphere contribution depends on four correlation times: the residence time of a water proton in the inner coordination sphere (τ_m), the rotational correlation time of the Mn···H vector (τ_R), and the electronic longitudinal and transverse relaxation rates of the metal ion ($1/T_{1e}$ and $1/T_{2e}$).[16] Additionally, the nuclear magnetic relaxation dispersion (NMRD) profiles recorded for $[Mn(H_2O)_6]^{2+}$ and $[Mn_2(ENOTA)]$ show an unusual dispersion at about 0.1 MHz that was attributed to an important scalar contribution to relaxivity, which depends on the hyperfine coupling constant, $A_H/\hbar$.[12] However, the NMRD profiles recorded for H_2NO2A derivatives containing different pendant arms did not show this second dispersion,[13] which points to a negligible scalar contribution to relaxivity.

The evaluation of the parameters influencing proton relaxivity in Mn^{2+}-based MRI CAs is normally achieved by analyzing the ^{1}H NMRD profiles recorded at different temperatures in conjunction with variable temperature ^{17}O NMR measurements of chemical shifts and transverse relaxation rates. Both the ^{17}O NMR chemical shifts and relaxation rates depend on the hyperfine coupling constant, $A_O/\hbar$, which has been found to fall within the range $(32-40) \times 10^6$ rad·s^{-1} for the Mn^{2+} complexes reported to date.[7−15] Both $A_O/\hbar$ and $A_H/\hbar$ are related to the difference between majority spin (α) and minority spin (β) densities at the corresponding nucleus, which can be evaluated by using ab initio computational methods[17] and density functional theory (DFT).[18,19] It has been shown recently that DFT calculations provide $A_O/\hbar$ values for Gd^{3+} complexes in very good agreement with the experimental data. Furthermore, these calculations showed that ^{1}H hyperfine coupling constants of coordinated water molecules take values close to zero, indicating that the scalar contribution to relaxivity can be safely negleted.[20,21]

In this Article, we present a combined experimental and computational study that aims at gaining information on the hyperfine coupling constants that govern the scalar contribution to ^{1}H relaxivity and the ^{17}O NMR chemical shifts and relaxation rates. For that purpose, following a new synthetic pathway, we have prepared and investigated the H_2MeNO2A (1,4-bis(carboxymethyl)-7-methyl-1,4,7-triazacyclononane) ligand, a triazacyclononane (TACN)-based macrocyclic chelator bearing one methyl group and two chelating acetate functions. Several reasons prompted us to prepare this particular ligand. First, on the basis of the results reported for $[Mn_2(ENOTA)(H_2O)_2]$, its Mn^{2+} complex is expected to contain an inner-sphere water molecule coordinated to the metal ion. Second, we wanted to check whether the substantial scalar contribution to relaxivity observed for $[Mn_2(ENOTA)(H_2O)_2]$ is also operating for the complex with $MeNO2A^{2-}$. Finally, one should bear in mind that the number of Mn^{2+} complexes investigated to date using ^{1}H and ^{17}O NMR measurements is rather limited, particularly considering the huge number of Gd^{3+} complexes characterized in the last 20 years. Therefore, this work represents also a part of our efforts to enlarge the number of Mn^{2+} complexes for which the parameters governing their relaxivity have been determined. This will allow establishment of relationships between the microscopic parameters related to the observed relaxivity, and the structure

dx.doi.org/10.1021/ic4014366 | Inorg. Chem. 2013, 52, 11173−11184

and dynamics of a particular complex, which eventually will lead to a rational design of Mn^{2+}-based contrast agents with improved relaxation properties.

Among the different organic tools available for selective N-alkylation of TACN,[22] we have chosen the orthoamide route[23] to obtain an easy and efficient synthesis of the ligand followed by its Mn^{2+} complexation. A full ^1H and ^{17}O relaxometric study was conducted to determine experimentally the ^1H and ^{17}O hyperfine coupling constants. DFT calculations were performed to gain information on the $A_O/\hbar$ and $A_H/\hbar$ hyperfine coupling constants and the relation between their values and the solution structure and dynamics of the complex. For comparative purposes, calculations were also performed on the well-known $[Mn(EDTA)(H_2O)]^{2-}$ complex. Finally, the $A_O/\hbar$ and $A_H/\hbar$ hyperfine coupling constants calculated for a series of Mn^{2+} complexes relevant as MRI CAs are compared with available experimental data.

EXPERIMENTAL SECTION

Materials and Methods. Reagents were purchased from ACROS Organics and from Aldrich Chemical Co. 1,4,7-Triazacyclononane (TACN) was purchased from CheMatech (Dijon, France). Acetonitrile, tetrahydrofurane, and toluene were distilled before use. ^1H and ^{13}C NMR spectra were recorded with a Bruker AMX-3 300 (300 MHz) spectrometer at the "Services communs" of the University of Brest.

*1-Methyl-1,4,7-triazacyclononane (**3**).* *N*-Dimethoxymethyl-*N*,*N*-dimethylamine (406 mg, 3.4 mmol, 1.1 equiv) was added to a solution of TACN (400 mg, 3.10 mmol) in chloroform (1 mL) and toluene (8 mL). The solution was stirred at room temperature for 12 h. The solvent was then evaporated under reduced pressure to yield an oily product (410 mg, 2.94 mmol, yield 95%). A solution of methyl iodide (1.1 equiv, 3.2 mmol, 200 μL) in 10 mL of freshly distilled THF was added to the previously obtained crude product. The mixture was stirred at room temperature for 4 days; the precipitated white solid was filtered, washed with THF, and dried under vacuum (660 mg, yield 80%). NMR (D_2O, ppm) ^1H 3.31 (m, 7H, CH_2 + CH_3) 3.75 (m, 8H, CH_2) 5.56 (s, 1H, C*H*); ^{13}C 51.2 (CH_3) 54.3 57.1 63.9 (CH_2) 121.6 (CH). The white solid was dissolved in 10 mL of a solution of methanol/HCl 12 M (1/1) and stirred under reflux for 12 h. After cooling, pH was raised to 12 by addition of NaOH pellets. Extraction with chloroform (3 × 15 mL), drying with $MgSO_4$, and evaporation of the solvent under reduced pressure gave 1-methyl-1,4,7-triazacyclononane (**3**) as a yellow oil (258 mg, 1.8 mmol, 77%). NMR ($CDCl_3$, ppm) ^1H 2.12 (s, 3H, CH_3) 2.27 (m, 4H, CH_2) 2.50 (m, 8H, CH_2) 2.77 (bs, 2H, N*H*); ^{13}C 44.5 (CH_3) 45.5 45.7 53.9 (CH_2).

*1,4-Bis(ethoxycarbonylmethyl)-7-methyl-1,4,7-triazacyclononane (**4**).* Compound **3** (143 mg, 1.0 mmol) was dissolved in 10 mL of freshly distilled acetonitrile, and 2 equiv of ethyl bromoacetate (2.0 mmol, 221 μL) and K_2CO_3 (3eq, 830 mg) were added. After stirring at room temperature for 5 days, the solution was filtered. Evaporation of the solvent gave a oily crude product. Purification was performed by column chromatography on neutral alumina Al_2O_3 (elution with $CHCl_3$ followed by $CHCl_3$/MeOH 99/1). Compound **4** was obtained as a yellow oil (110 mg, 40%). NMR ($CDCl_3$, ppm) ^1H 1.20 (t, 6H, CH_3CH_2) 2.40 (s, 3H, CH_3-N) 2.83−2.88 (m, 12H, CH_2-N) 3.39 (s, 4H, CH_2-N) 4.09 (q, 4H, CH_2CH_3); ^{13}C 14.2 (CH_3CH_2) 45.8 (N-CH_3) 54.4 55.3 55.9 (CH_{2tacn}) 58.7 (CH_2CH_3) 60.1 (CH_2−N).

1,4-Bis(carboxymethyl)-7-methyl-1,4,7-triazacyclononane (MeNO2A). Compound **4** (100 mg, 0.35 mmol) was dissolved in 8 mL of HCl 6 M and heated under reflux for 12 h. Evaporation of the aqueous phase gave a hygroscopic white solid corresponding to 1,4-bis(carboxymethyl)-7-methyl-1,4,7-triazacyclononane (H_2MeNO2A) in its hydrochloride form (115 mg, 90%). NMR (D_2O, ppm) ^1H 2.97 (s, 3H, CH_3) 3.30 (m, 4H, CH_{2tacn}) 3.44 (m, 4H, CH_{2tacn}) 3.56 (m, 4H, CH_{2tacn}) 3.91 (s, 4H, CH_2COOH); ^{13}C 47.5 (CH_3) 52.4 53.8 55.2 (CH_{2tacn}) 59.5 (CH_2COOH) 174.5 (COOH).

^1H and ^{17}O NMR Measurements. The proton $1/T_1$ NMRD profiles were measured on a fast field-cycling Stelar SmartTracer relaxometer (Mede, Pv, Italy) over a continuum of magnetic field strengths from 0.00024 to 0.25 T (corresponding to 0.01−10 MHz proton Larmor frequencies). The relaxometer operates under computer control with an absolute uncertainty in $1/T_1$ of ±1%. The temperature was controlled with a Stelar VTC-91 airflow heater equipped with a calibrated copper−constantan thermocouple (uncertainty of ±0.1 K). Additional data points in the range 15−70 MHz were obtained on a Stelar relaxometer equipped with a Bruker WP80 NMR electromagnet adapted to variable-field measurements (15−80 MHz proton Larmor frequency). For these ^1H data, a 5.5 mM solution of the Mn^{2+} complex in nondeuterated water was utilized. The exact complex concentration was determined by the BMS shift method at 11.7 T. ^{17}O NMR measurements were recorded on a Bruker Avance III spectrometer (11.7 T) equipped with a 5 mm probe and standard temperature control unit. A 7.0 mM aqueous solution of the complex containing 2.0% of the ^{17}O isotope (Cambridge Isotope) was used. The observed transverse relaxation rates were calculated from the signal width at half-height.

Theory. The isotropic Fermi contact contribution (A_{iso}) of the hyperfine coupling tensor for a nucleus N is given by[24]

$$A_{iso}(N) = \frac{4\pi}{3S}\beta_e\beta_N g_e g_N \rho^{\alpha-\beta}(R_N) \quad (1)$$

where β_N and β_e are the nuclear and Bohr magnetons, respectively, g_N and g_e are nuclear and free-electron g values, S is the total spin of the system, and $\rho^{\alpha-\beta}$ represents the difference between majority spin (α) and minority spin (β) densities. Experimental values of isotropic ^{17}O HFCCs have been determined for a relatively small number of Mn^{II} complexes from transverse ^{17}O NMR relaxation rates and chemical shifts. The reduced transverse relaxation rates and chemical shift, $1/T_{2r}$ and ω_r, may be written as in eqs 2 and 3,[25] where $1/T_{2m}$ is the relaxation rate of the bound water, τ_m is the residence time of water molecules in the inner sphere, $\Delta\omega_m$ is the chemical shift difference between bound and bulk water, and $\Delta\omega_{os}$ is the outer sphere contribution to the chemical shift.

$$\frac{1}{T_{2r}} = \frac{1}{\tau_m}\frac{T_{2m}^{-2} + \tau_m^{-1}T_{2m}^{-1} + \Delta\omega_m^2}{(\tau_m^{-1} + T_{2m}^{-1})^2 + \Delta\omega_m^2} \quad (2)$$

$$\Delta\omega_r = \frac{\Delta\omega_m}{(1 + \tau_m T_{2m}^{-1})^2 + \tau_m^2\Delta\omega_m^2} + \Delta\omega_{os} \quad (3)$$

$\Delta\omega_m$ is determined by the ^{17}O hyperfine or scalar coupling constant, $A_O/\hbar$, according to eq 4, where **B** represents the magnetic field, S is the electron spin, and g_L is the isotropic Landé g factor.[26]

$$\Delta\omega_m = \frac{g_L\mu_B S(S+1)\mathbf{B}}{3k_B T}\frac{A_O}{\hbar} \quad (4)$$

The transverse ^{17}O NMR relaxation is dominated by the scalar contribution, $1/T_{2sc}$, as given in eq 5:[27]

$$\frac{1}{T_{2m}} \cong \frac{1}{T_{2sc}} = \frac{S(S+1)}{3}\left(\frac{A_O}{\hbar}\right)^2\left(\tau_{s1} + \frac{\tau_{s2}}{1 + \tau_{s2}^2\omega_s^2}\right) \quad (5)$$

where $1/\tau_{si}$ is the sum of the exchange rate constant and the longitudinal ($1/T_{1e}$) or transverse ($1/T_{2e}$) electron spin relaxation rates:

$$\frac{1}{\tau_{si}} = \frac{1}{\tau_m} + \frac{1}{T_{ie}} \quad (6)$$

Thus, both the ^{17}O NMR chemical shifts and transverse relaxation rates depend on the HFCC $A_O/\hbar$, among other parameters.

The scalar contribution to ^1H relaxivity is given by the following equation:

dx.doi.org/10.1021/ic4014366 | Inorg. Chem. 2013, 52, 11173−11184

$$\frac{1}{T_1^{SC}} = \frac{2S(S+1)}{3}\left(\frac{A_H}{\hbar}\right)^2\left(\tau_{s1} + \frac{\tau_{s2}}{1+\tau_{s2}^2\omega_s^2}\right) \quad (7)$$

Where $A_H/\hbar$ is the ^{1}H hyperfine or scalar coupling constant. In eqs 4, 5, and 7, $A_O/\hbar$ and $A_H/\hbar$ are expressed in rad·s^{-1}, and therefore equal $2\pi A_{iso}$ as defined in eq 1.

Computational Methods. All calculations presented in this work were performed employing the Gaussian 09 package (revision B.01).[28] Full geometry optimizations of the $[Mn(MeNO2A)(H_2O)]\cdot xH_2O$ and $[Mn(EDTA)(H_2O)]^{2-}\cdot xH_2O$ systems (x = 0–4) were performed in aqueous solution employing DFT within the hybrid generalized gradient approximation (hybrid GGA) with the B3LYP exchange correlation functional[29,30] and within the hybrid meta-GGA approximation with the TPSSh exchange-correlation functional.[31] Input geometries were generated from the crystallographic data of $[Mn(EDTA)(H_2O)]^{2-}$ and $[Mn_2(ENOTA)(H_2O)]\cdot 5H_2O$ complexes. For geometry optimization purposes, we used the standard Ahlrichs' valence double-ξ basis set including polarization functions (SVP).[32] The same computational approaches were used for geometry optimizations of the $[Mn(CyDTA)(H_2O)]^{2-}\cdot 4H_2O$, $[Mn(L1)(H_2O)]\cdot 4H_2O$, $[Mn(L2)(H_2O)]^{+}\cdot 4H_2O$, $[Mn(L3)(H_2O)_2]^{2+}\cdot 8H_2O$, and $[Mn_2(ENOTA)(H_2O)_2]\cdot 8H_2O$ systems. The corresponding X-ray structures were used to construct input geometries for geometry optimization purposes. No symmetry constraints have been imposed during the optimizations. The highest spin state was considered as the ground state (sextuplet, $3d^5$) in all cases. Since these calculations were performed by using an unrestricted model, spin contamination[33] was assessed by a comparison of the expected difference between $S(S+1)$ for the assigned spin state ($S(S+1)$ = 8.75 for the mononuclear Mn^{II} complexes investigated here) and the actual value of $\langle S^2\rangle$.[34] The results obtained indicate that spin contamination is negligible for systems investigated in this work [$\langle S^2\rangle - S(S+1) < 0.0050$]. The stationary points found on the potential energy surfaces as a result of geometry optimizations were tested to represent energy minima rather than saddle points via frequency analysis.

The geometries of the $[Mn(EDTA)(H_2O)]^{2-}\cdot 4H_2O$, $[Mn(CyDTA)(H_2O)]^{2-}\cdot 4H_2O$, $[Mn(L2)(H_2O)]^{+}\cdot 4H_2O$, $[Mn(L3)(H_2O)_2]^{2+}\cdot 8H_2O$, and $[Mn_2(ENOTA)(H_2O)_2]\cdot 8H_2O$ systems show a very good agreement with reference crystallographic data. The agreement between the bond distances obtained with DFT calculations and those observed in the solid state was assessed by using the unsigned mean error (UME), as given by eq 8:

$$\mathrm{UME} = \frac{1}{n}\sum_{i=1}^{n} |D_{X\text{-}ray} - D_{DFT}| \quad (8)$$

where $D_{X\text{-}ray}$ and D_{DFT} are the experimental and calculated distances, respectively.

The UME values shown in Figure 1 indicate that B3LYP provides a poorer agreement with the experimental data than TPSSh for all systems investigated, with average UME values of 0.042 and 0.025 Å at the B3LYP/SVP and TPSSh/SVP levels, respectively. A closer inspection of the bond distances shows that the better performance of TPSSh compared with B3LYP is mainly related to large deviations of the calculated Mn–N distances obtained from B3LYP calculations (Figure 1), as previously observed in the case of lanthanide complexes.[35] The poor performance of B3LYP compared with TPSSh to reproduce the experimental Ln–N distances is in line with previous investigations that found serious failures of the B3LYP functional that may arise from design problems[36] (i.e., B3LYP was shown to fail to provide accurate geometries of iron porphyrins).[37] Thus, we used the TPSSh functional for the calculation of HFCCs and ab initio molecular dynamics (AIMD) simulations.

Isotropic ^{17}O and ^{1}H HFCCs in the $[Mn(MeNO2A)(H_2O)]\cdot xH_2O$, $[Mn(EDTA)(H_2O)]^{2-}\cdot xH_2O$ (x = 0–4), $[Mn(CyDTA)(H_2O)]^{2-}\cdot 4H_2O$, $[Mn(L1)(H_2O)]\cdot 4H_2O$, $[Mn(L2)(H_2O)]^{-}\cdot 4H_2O$, and $[Mn(L3)(H_2O)_2]^{2+}\cdot 8H_2O$ systems were calculated in aqueous solution with unrestricted DFT methods by employing the TPSSh exchange–correlation functional. In all DFT investigations of HFCCs specifically developed basis sets with extra flexibility in the core region should be employed.[38] Thus, for the description of C, H, N, and O, we used the EPR-III basis set of Barone,[39] which is a triple-ζ basis set including diffuse functions, double d-polarizations, and a single set of f-polarization functions, together with an improved s-part to better describe the nuclear region. For Mn, we used the standard Ahlrichs' valence triple-ξ basis set including polarization functions (TZVP).[40]

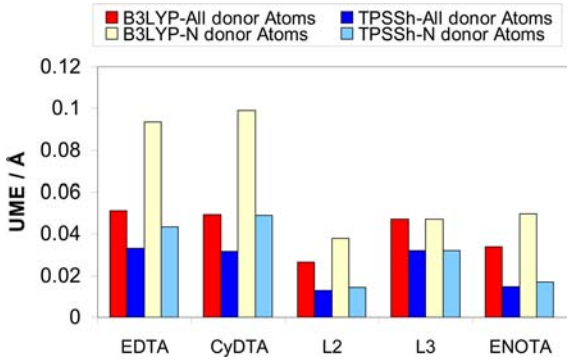

Figure 1. Unsigned mean error (UME) values (Å) obtained for $[Mn(EDTA)(H_2O)]^{2-}\cdot 4H_2O$, $[Mn(CyDTA)(H_2O)]^{2-}\cdot 4H_2O$, $[Mn(L2)(H_2O)]^{+}\cdot 4H_2O$, $[Mn(L3)(H_2O)_2]^{2+}\cdot 8H_2O$, and $[Mn_2(ENOTA)(H_2O)_2]\cdot 8H_2O$ compared with reference crystallographic data.

Convergence of the SCF procedure during geometry optimization and calculations of HFCCs was found to be problematic in some cases, and thus we used a quadratically convergent SCF procedure when first-order SCF did not achieve convergence (by using the scf = xqc keyword in g09). The default values for the integration grid (75 radial shells and 302 angular points) and the SCF energy convergence criteria (10^{-8}) were used in all calculations.

Classical trajectory calculations were performed in aqueous solution at the TPSSh/SVP level by using the atom centered density matrix propagation (ADMP) molecular dynamics model.[41] Time steps of 0.2 fs were used during the simulations, and a total of 3000 and 4000 steps were run for the trajectory simulations of $[Mn(MeNO2A)(H_2O)]\cdot 4H_2O$ and $[Mn(EDTA)(H_2O)]^{2-}\cdot 4H_2O$, respectively. The fictitious electron mass was 0.1 amu. All the ADMP calculations were started from the corresponding optimized geometries obtained as described above.

Throughout this work, solvent effects were included by using the polarizable continuum model (PCM), in which the solute cavity is built as an envelope of spheres centered on atoms or atomic groups with appropriate radii. In particular, we used the integral equation formalism (IEFPCM) variant as implemented in Gaussian 09.[42]

RESULTS AND DISCUSSION

Synthesis of the H_2MeNO2A ligand. The synthesis of ligand H_2MeNO2A has been achieved by using the already known orthoamide route.[23] Five steps allowed us to obtain the ligand starting from triazacyclononane (TACN, Scheme 1). The formation of the 1,4,7-triazatricyclo[5.2.1.0^{4,10}]decane derivative **1** was initiated by reaction of TACN with *N*-dimethoxymethyl-*N*,*N*-dimethylamine. Addition of methyl iodide to the obtained orthoamide **1** gave rise to the precipitation of the corresponding monoammonium salt **2** in tetrahydrofurane. An acidic hydrolysis in methanolic medium followed by basic treatment of the solution has been preferred to the alkaline hydrolysis of the same intermediate used by Peacock and colleagues[43] for the synthesis of 1-methyl-1,4,7-triazacyclononane **3**. Reaction of **3** with ethyl bromoacetate in S_N2 conditions allowed the alkylation of the secondary amine functions with an ethyl acetate group. Hydrolysis with a HCl 6 M solution gave the final ligand MeNO2A in its hydrochloride salt form.

dx.doi.org/10.1021/ic4014366 | Inorg. Chem. 2013, 52, 11173–11184

Scheme 1. Four-Step Synthesis of H_2MeNO2A[a]

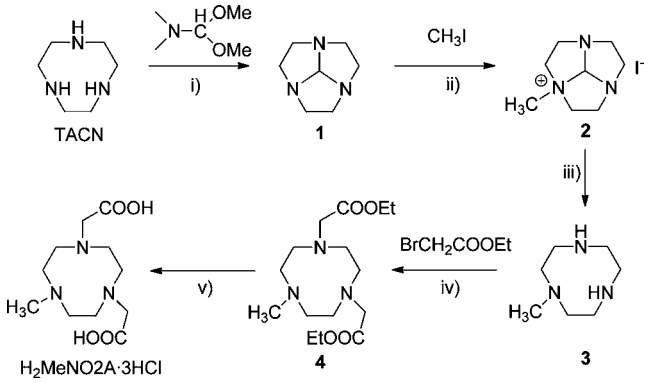

[a]Reagents and conditions: (i) $CHCl_3$/toluene, RT, 12 h, 95%; (ii) THF, 4 days, 80%; (iii) HCl 6 M/MeOH, Δ, 12 h, then OH^-, 77%; (iv) CH_3CN, K_2CO_3, RT, 5 days, 40%; (v) HCl 6 M, Δ, 12 h, 90%.

Variable Temperature NMRD and ^{17}O NMR Measurements. Nuclear magnetic relaxation dispersion (NMRD) profiles of an aqueous solution of [Mn(MeNO2A)(H_2O)] (pH = 7.2) were measured at 283, 298, and 310 K in the proton Larmor frequency range 0.01−70 MHz, corresponding to magnetic field strengths varying between 2.343×10^{-4} and 1.645 T (Figure 2). The relaxivity of [Mn(MeNO2A)(H_2O)]

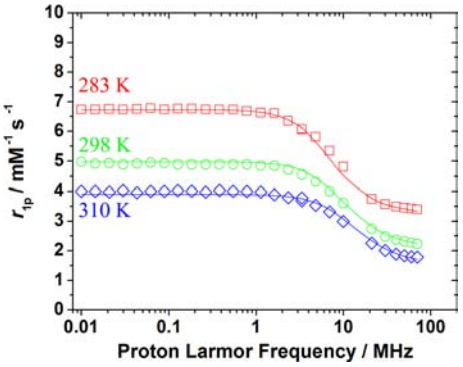

Figure 2. ^{1}H NMRD profiles recorded at different temperatures for [Mn(MeNO2A)(H_2O)]. The lines represent the fit of the data as explained in the text.

decreases with increasing temperature, a behavior typical of small chelates in which fast rotation of the complex in solution limits proton relaxivity (Figure 2, see also Figure S5, Supporting Information). The ^{1}H NMRD profiles show a single dispersion between 1 and 10 MHz, while the second dispersion at ∼0.1 MHz characteristic of an important scalar contribution to relaxivity is not observed. The inner-sphere contribution to relaxivity is directly proportional to the number of inner-sphere water molecules (q), and therefore relaxivity values provide information on the hydration level of Mn^{2+} complexes providing they possess comparable molecular weights and electronic relaxation times. As expected, the relaxivity of [Mn(MeNO2A)(H_2O)] (2.74 $mM^{-1}\cdot s^{-1}$ at 20 MHz and 298 K) is quite similar to those of Mn^{2+} complexes containing an inner-sphere water molecule.[10]

The reduced transverse ^{17}O relaxation rates and chemical shifts measured for [Mn(MeNO2A)(H_2O)] are presented in Figure 3. For [Mn(MeNO2A)(H_2O)], $1/T_{2r}$ increases with decreasing temperature, which indicates that the system is in

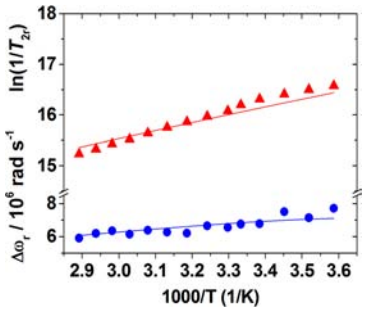

Figure 3. Reduced transverse (▲) ^{17}O relaxation rates and ^{17}O chemical shifts (●) measured for [Mn(MeNO2A)(H_2O)] at 11.74 T. The lines represent the fit of the data as explained in the text.

the fast exchange regime over the whole range of temperatures investigated, suggesting a relatively short residence time of the inner-sphere water molecule.

A simultaneous fitting of the NMRD and ^{17}O NMR data of [Mn(MeNO2A)(H_2O)] was performed with the sets of equations given in the Supporting Information. Some parameters were fixed during the fitting procedure: the distance of closest approach for the outer-sphere contribution a_{MnH} was fixed at 3.6 Å,[44] while the distance between the proton nuclei of the coordinated water molecule and the Mn^{2+} ion (r_{MnH}) was fixed at 2.772 Å. This value corresponds to the mean Mn···H distance obtained during the course of our molecular dynamics simulations described below. The number of water molecules in the inner coordination sphere of Mn^{2+} was fixed to q = 1. The parameters obtained from the fittings are listed in Table 1,

Table 1. Parameters Obtained from the Simultaneous Analysis of ^{17}O NMR and NMRD Data

	MeNO2A	ENOTA[b]	EDTA[c]	1,4-DO2A[c]
k_{ex}^{298}, 10^6 s^{-1}	626 ± 23	55.0	471	1134
$\Delta H^{\ddagger}$, kJ mol^{-1}	11 ± 1.0	20.5	33.5	29.4
τ_R^{298}, ps	36 ± 3	85	57	46
E_r, kJ mol^{-1}	22.8 ± 0.7	18	21.8	19.1
τ_v^{298}, ps	21.4 ± 3.8	7.7	27.9	4.4
E_v, kJ mol^{-1}	1.0[a]	24.8	1.0[a]	1.0[a]
D_{MnH}^{298}, 10^{-10} m^2 s^{-1}	26.9 ± 4.0	23	23.1	23.0[a]
E_{DMnH}, kJ mol^{-1}	17.3 ± 2.4	18	18.9	17.3[a]
Δ^2, 10^{19} s^{-2}	7.2 ± 1.5	0.47	6.9	48.1
$A_O/\hbar$, 10^6 rad s^{-1}	46.0 ± 0.2	32.7	40.5	43.0[a]
r_{MnH}, Å	2.77[a]	2.75	2.83[a]	2.83[a]
a_{MnH}, Å	3.6[a]	3.2	3.6[a]	3.6[a]
q^{298}	1[a]	1[a]	1[a]	0.87

[a]Parameters fixed during the fitting procedure. The value of the activation energy for the activation energy related to the correlation time for the modulation of the zero-field-splitting (E_v) was fixed to a small positive value (1 kJ mol^{-1}); otherwise negative activation energies were obtained. [b]Reference 12. [c]Reference 10.

while the curve fits are shown in Figures 2 and 3. The analysis of the NMRD and ^{17}O NMR data including $A_H/\hbar$ as a fitting parameter did not improve the quality of the fitting, which suggests that the scalar contribution to relaxivity is negligible in this case. The values obtained for the diffusion coefficient, D_{MnH}^{298}, and its activation energy, E_{DMnH}, are close to those for self-diffusion of water molecules in pure water: $D^{298} = 2.3 \times 10^{-9}$ $m^2\cdot s^{-1}$ and E_D = 17.3 kJ·mol^{-1},[45] indicating that they are dominated by the rapid diffusion of water molecules. The value

dx.doi.org/10.1021/ic4014366 | Inorg. Chem. 2013, 52, 11173−11184

of the rotational correlation time (τ_R^{298}) obtained from the analysis of the ^{1}H NMRD profiles is very similar to those reported for small Mn(II) complexes, but clearly smaller than that reported for the binuclear $[Mn_2(ENOTA)(H_2O)_2]$ complex. The relatively low τ_R^{298} value obtained for the complex of MeNO2A (36 ps) is in line with the lower molecular weight of this complex in comparison to the 1,4-DO2A and EDTA analogues.

The water exchange rate (k_{ex}^{298}) determined for $[Mn(MeNO2A)(H_2O)]$ is similar to that determined previously for the complex of EDTA, but slower than in the complex of 1,4-DO2A, which presents an equilibrium in solution between a $q = 1$ species and a six-coordinated $q = 0$ form. The values of the mean square zero-field-splitting energy (Δ^2) and the electronic correlation time for the modulation of the zero-field-splitting (τ_V^{298}) obtained for the complexes with MeNO2A and EDTA are very similar, indicating that these complexes possess very similar electronic relaxation times. Finally, the value obtained for the ^{17}O hyperfine coupling constant ($A_O/\hbar = (46.0 \pm 0.2) \times 10^6$ rad·s^{-1}, which corresponds to a A_{iso} value of −7.30 MHz) is very similar to the values obtained for the complex of EDTA and different Mn^{2+} complexes with polyaminocarboxylate ligands.[10] The water exchange rate determined for $[Mn(MeNO2A)(H_2O)]$ is 1 order of magnitude faster than that reported for the complex with ENOTA, while the parameters related to the electronic relaxation in both systems are also very different. This highlights how small structural differences may have an important impact on the parameters governing the relaxivity in Mn^{2+} complexes.

Molecular Geometries of $[Mn(MeNO2A)(H_2O)]$ and $[Mn(EDTA)(H_2O)]^{2-}$ Complexes. Our previous work performed on Gd^{3+} and Mn^{2+} complexes with polyaminocarboxylate ligands showed that the explicit inclusion of a few second-sphere water molecules is crucial for the computation of accurate distances between the metal ion and the oxygen atom of coordinated water molecules in these systems.[10,21] Indeed, geometry optimizations performed on the $[Mn(EDTA)(H_2O)]^{2-}$ complex at the TPSSh/SVP level provided a Mn−O_{water} distance of 2.524 Å. This distance is ca. 0.3 Å longer than that observed in the X-ray crystal structure (2.241 Å).[46] However, geometry optimizations performed on the $[Mn(EDTA)(H_2O)]^{2-}\cdot 4H_2O$ system, which explicitly includes four second-sphere water molecules, reduced the Mn−O_{water} distance to 2.302 Å, in considerably better agreement with the experimental value observed in the solid state. Geometry optimizations performed on the $[Mn(EDTA)(H_2O)]^{2-}\cdot xH_2O$, and $[Mn(MeNO2A)(H_2O)]\cdot xH_2O$ systems ($x = 0-5$) confirm the importance of explicitly including the most important interactions involving inner- and second-sphere water molecules (Figure 4). Indeed, the inclusion of up to two second-sphere water molecules provokes important variations on the calculated Mn−O_{water} distances. In the case of $[Mn(EDTA)(H_2O)]^{2-}\cdot xH_2O$, this distance shortens by 0.26 Å on increasing x from 0 to 2, while for $[Mn(MeNO2A)(H_2O)]\cdot xH_2O$, the Mn−$O_{water}$ distances changes by 0.13 Å. Adding a third water molecule to the second solvation shell results in an increase of the Mn−O_{water} distances by 0.03−0.06 Å, while the impact of adding a fourth or a fifth second-sphere water molecule is relatively small (<0.025 Å). The important effect that inclusion of second-sphere water molecules has on the Mn−O_{water} distances is attributed to the fact that continuum models of solvation cannot account for specific solvent−solute interactions, such as the hydrogen-bonding interactions involving inner-sphere and second-sphere water molecules.[47] The data shown in Figure 4 indicate that a mixed cluster/continuum approach explicitly including three to five second-sphere water molecules is required to overcome this deficiency of continuum solvent models to describe Mn^{II} complexes that have concentrated charge densities and strong local solute−solvent interactions.

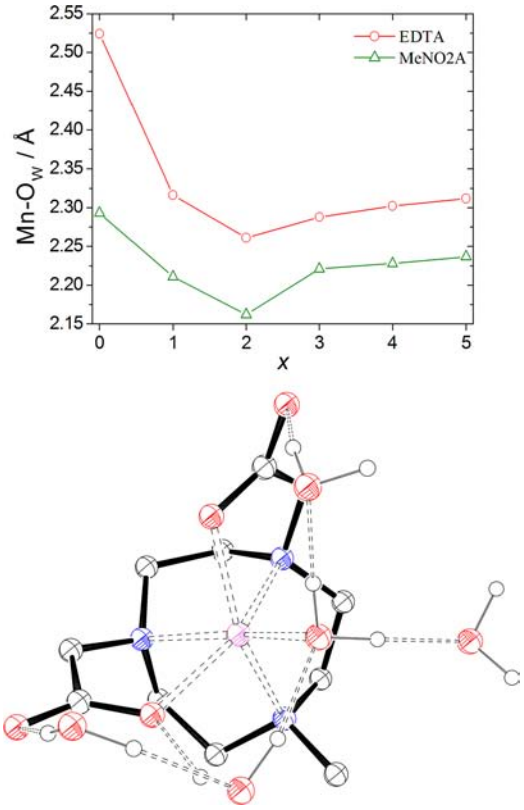

Figure 4. (top) Distances between Mn and the oxygen atoms of inner-sphere water molecules calculated for $[Mn(MeNO2A)(H_2O)]\cdot xH_2O$ and $[Mn(EDTA)(H_2O)]^{2-}\cdot xH_2O$ at the TPSSh/SVP level (x represents the number of noncoordinated water molecules). (bottom) Geometry of the $[Mn(MeNO2A)(H_2O)]\cdot 4H_2O$ system optimized at the TPSSh/SVP level.

The optimized geometry of the $[Mn(MeNO2A)(H_2O)]\cdot 4H_2O$ system is shown in Figure 4. Three of the second-sphere water molecules are involved in hydrogen-bonding interactions with the coordinated water molecule, while the fourth one is hydrogen-bonded to a second-sphere water and a carboxylate group. Thus, at least three second-sphere water molecules appear to be required to account for hydrogen-bonding interactions involving the coordinated water molecule and the second solvation shell, while addition of extra water molecules to the system does not substantially affect the Mn−O_{water} bond distance. As expected, the metal ion in $[Mn(MeNO2A)(H_2O)]\cdot 4H_2O$ is six coordinated, being directly bound to the three nitrogen atoms of the TACN unit (Mn−N distances in the range 2.30−2.37 Å), two oxygen atoms of the carboxylate groups (Mn−O distances 2.127 and 2.113 Å), and the coordinated water molecule. These distances are in excellent agreement with those observed in the solid state for ENOTA complex, which shows average Mn−O and Mn−N distances of 2.124 and 2.308 Å, respectively.[12]

dx.doi.org/10.1021/ic4014366 | Inorg. Chem. 2013, 52, 11173−11184

To investigate the relative stability of the six- and seven-coordinated forms of the $[Mn(MeNO2A)(H_2O)_q]$ complex (q = 1 or 2), we have performed a relaxed potential-energy surface scan of the $[Mn(MeNO2A)(H_2O)]\cdot 4H_2O$ system. The distance between Mn and an oxygen atom of a second-sphere water molecule was varied in steps of 0.1 Å between 4.07 and 2.97 Å, generating 22 points. These calculations indicated that the hypothetical $[Mn(MeNO2A)(H_2O)_2]\cdot 3H_2O$ species is not a minimum on the PES, because approaching a second-sphere water molecule to the metal ion results in the expulsion of the coordinated water molecule.

Calculation of ^{17}O and ^{1}H HFCCs of the Coordinated Water Molecule in $[Mn(MeNO2A)(H_2O)]$ and $[Mn(EDTA)(H_2O)]^{2-}$ Complexes. The ^{17}O and ^{1}H A_{iso} values of the inner sphere water molecule in the $[Mn(MeNO2A)(H_2O)]\cdot xH_2O$ and $[Mn(EDTA)(H_2O)]^{2-}\cdot xH_2O$ systems were calculated with the aid of the TPSSh functional, which has been shown to provide accurate HFCCs for Gd^{3+} complexes (Table 2).[21]

Table 2. Calculated ^{17}O and ^{1}H Hyperfine Coupling Constants (A_{iso}, MHz) for the $[Mn(MeNO2A)(H_2O)]\cdot xH_2O$ and $[Mn(EDTA)(H_2O)]^{2-}\cdot xH_2O$ systems

	EDTA		MeNO2A	
	^{17}O	$^{1}H^{a}$	^{17}O	$^{1}H^{a}$
x = 0	−2.603	0.035(13)	−7.793	0.870(421)
x = 1	−4.971	0.182(57)	−7.931	1.170(324)
x = 2	−6.471	0.472(83)	−7.604	1.376(298)
x = 3	−6.301	0.395(83)	−6.341	0.930(161)
x = 4	−6.041	0.364(79)	−5.902	0.851(63)
	−5.94[d]	0.350[d]	−5.98[d]	0.865[d]
expt	−6.45[b]		−7.30[c]	

[a]Averaged values are provided with standard deviations in parentheses. [b]Reference 10. [c]This work. [d]Calculated values obtained from the analysis of the trajectories of ADMP simulations (see text).

Calculations performed on the $[Mn(EDTA)(H_2O)]^{2-}$ system provided a ^{17}O A_{iso} value that deviates considerably from the corresponding experimental values. However, the inclusion of two or more second-sphere water molecule pushes the calculated values closer to the experimental ones. The effect of including second-sphere water molecules for the $[Mn(MeNO2A)(H_2O)]$ complex is not as important, most likely due to the smaller electric charge of the complex, which probably results in weaker hydrogen-bonding interactions between the coordinated water and negatively charged groups of the ligand. For the systems containing four second-sphere water molecules (x = 4), a good agreement with the experiment is observed, the computed values differing by only ∼6% and 19% with respect to the experimental ones for the complexes of EDTA and MeNO2A, respectively. The data shown in Table 2 also indicate that the inclusion of second sphere water molecules has an important impact on the calculated ^{1}H A_{iso} values, which are considerably higher in the case of the MeNO2A complex than in the EDTA analogue. Thus, the explicit consideration of the most important hydrogen-bonding interaction involving the coordinated water molecule and the second-sphere coordination shell appears to be crucial for an accurate calculation of ^{17}O and ^{1}H A_{iso} values of the inner-sphere water molecule.

The measured HFCCs are weighted averages ($\langle A_{iso}\rangle$) of individual values for the different configurations present in solution, and therefore solution dynamics might have an important impact on the measured ^{1}H and ^{17}O A_{iso} values. Indeed, Yazyev et al. investigated the hyperfine interactions of ^{1}H and ^{17}O nuclei of inner-sphere water molecules in $[Gd(H_2O)_8]^{3+}$ and $[Gd(DOTA)(H_2O)]^{-}$ complexes.[20] The approach used by these authors to calculate the hyperfine interactions involved either classical or Car−Parrinello molecular dynamics (MD) simulations. From the trajectories of these simulations, clusters of molecules were extracted and then investigated by using DFT calculations, which provided ^{17}O hyperfine coupling constants in good agreement with the experimental values. Thus, we have followed a similar approach to investigate the effect of solution dynamics on the HFCCs of Mn^{2+} complexes with EDTA and MeNO2A. Among the different molecular dynamics methods available, we selected the atom-centered density matrix propagation (ADMP) approach, which exhibits $O(N)$ scaling of computational time with system size (N is the number of electrons),[48] making it a reasonable choice compared with other computationally more expensive ab initio molecular dynamics methods.

ADMP simulations were performed in aqueous solution at the TPSSh/SVP level and started on the equilibrium geometries of the $[Mn(MeNO2A)(H_2O)]\cdot 4H_2O$ and $[Mn(EDTA)(H_2O)]^{2-}\cdot 4H_2O$ systems. The overall simulation time was 600 fs for the MeNO2A complex and 800 fs for the EDTA analogue. The configuration space sampling (100 snapshots) was extracted from the corresponding trajectories at regular intervals of 6 and 8 fs for the MeNO2A and EDTA complexes, respectively. As expected, no water exchange events were observed during the simulations, because the residence time of coordinated water molecules in the Mn^{2+} coordination sphere is considerably longer than the simulation time. As pointed out previously,[21] two important parameters influence the ^{17}O HFCCs: the metal−O distance and the orientation of the water molecule plane with respect to the metal−O vector. Both the $Mn-O_{water}$ distance and the orientation of the water molecule given by the Mn−O−H−H dihedral angle fluctuate considerably during the length of our ADMP simulations (Figure 5). For $[Mn(MeNO2A)(H_2O)]\cdot 4H_2O$, the $Mn-O_{water}$ distance amounts to 2.228 Å at the beginning of the simulation and fluctuates between 2.089 and 2.325 Å during the simulation time. For the EDTA analogue, the $Mn-O_{water}$ distance varies between 2.430 and 2.217 Å during the course of the simulation. Concerning the Mn−O−H−H dihedrals, they oscillate

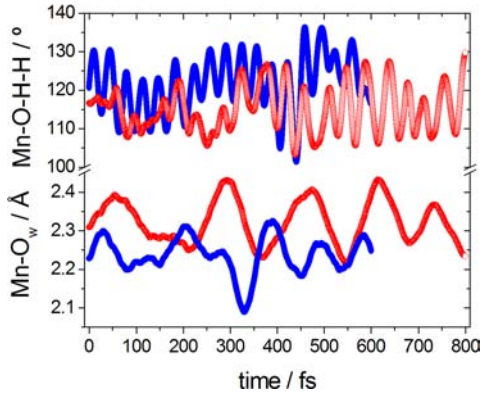

Figure 5. Calculated Mn−O distance and Mn−O−H−H dihedral angle during the full length of the ADMP simulations performed in aqueous solution on the $[Mn(MeNO2A)(H_2O)]\cdot 4H_2O$ (●, blue) and $[Mn(EDTA)(H_2O)]^{2-}\cdot 4H_2O$ (○, red) systems (TPSSh/SVP).

dx.doi.org/10.1021/ic4014366 | Inorg. Chem. 2013, 52, 11173−11184

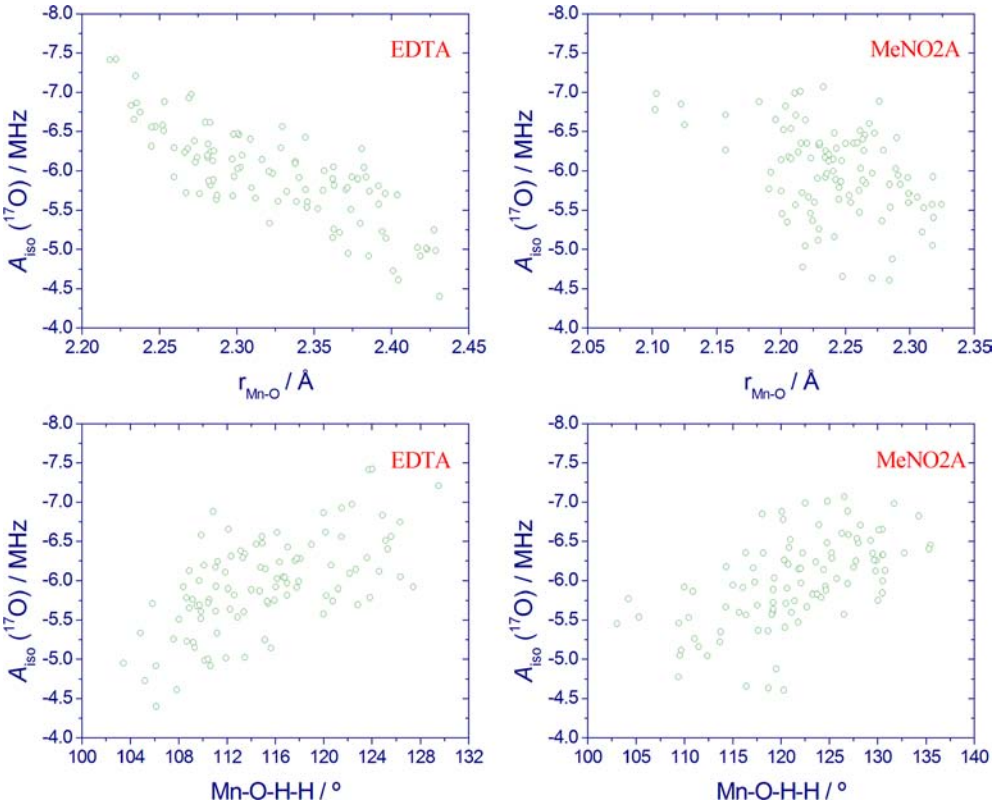

Figure 6. ^{17}O isotropic hyperfine coupling constant, A_{iso}, plotted as function of Mn−O_w distance (top), Mn−O−H−H dihedral angle (bottom) for 100 configurations extracted from MD trajectories of $[Mn(EDTA)(H_2O)]^{2-}\cdot 4H_2O$ (left) and $[Mn(MeNO2A)(H_2O)]\cdot 4H_2O$ (right).

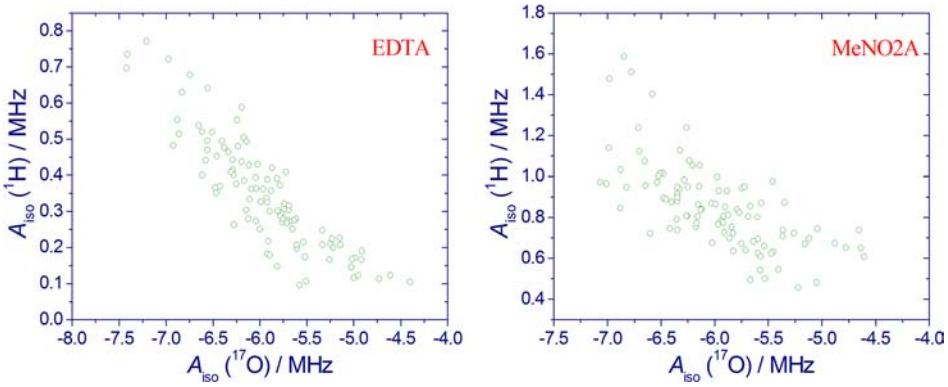

Figure 7. ^{17}O isotropic hyperfine coupling constant plotted as function of the ^{1}H hyperfine coupling constant for 100 configurations extracted from MD trajectories of $[Mn(EDTA)(H_2O)]^{2-}\cdot 4H_2O$ (left) and $[Mn(MeNO2A)(H_2O)]\cdot 4H_2O$ (right).

between 101.5° and 136.3° for the MeNO2A complex and between 103.2° and 129.7° for the EDTA one. Simulations performed on the $[Mn(MeNO2A)(H_2O)]$ system (Figure S6, Supporting Information), which does not include a second hydration shell, provide Mn−O_{water} distances varying between 2.158 and 2.489 Å during the simulation time (600 ps). Thus, the inclusion of an explicit second-sphere hydration shell not only results in shorter Mn−O_{water} distances but also reduces its fluctuation during the MD simulations.

The averaged ^{1}H and ^{17}O A_{iso} values ($\langle A_{iso}\rangle$) obtained from the 100 snapshots extracted from the trajectory calculated for $[Mn(MeNO2A)(H_2O)]\cdot 4H_2O$ amount to −5.98 ± 1.37 (^{17}O) and 0.865 ± 0.721 (^{1}H) MHz for an average Mn−O_{water} distance of 2.239 Å and an average Mn−O−H−H dihedral of 121.70°. In the case of the $[Mn(EDTA)(H_2O)]^{2-}\cdot 4H_2O$ system, our calculations provide $\langle A_{iso}\rangle$ values of −5.95 ± 1.54 (^{17}O) and 0.374 ± 0.424 (^{1}H) MHz for an averaged Mn−O_{water} distance of 2.318 Å and an average Mn−O−H−H dihedral of 115.07°. The large standard deviations of the $\langle A_{iso}\rangle$ values show that the calculated A_{iso} values change significantly during the course of the simulations, as a consequence of important changes in both the Mn−O_{water} distance and the orientation of the coordinated water molecule.

Figure 6 shows plots of the ^{17}O A_{iso} values, calculated for each of the 100 snapshots extracted from the trajectory calculations performed on the $[Mn(MeNO2A)(H_2O)]\cdot 4H_2O$ and $[Mn(EDTA)(H_2O)]^{2-}\cdot 4H_2O$ systems versus the Mn−O_W distance and the Mn−O−H−H dihedral angles. These plots show rough linear trends that indicate that short Mn−O_w distances and large Mn−O−H−H dihedral angles favor larger

dx.doi.org/10.1021/ic4014366 | Inorg. Chem. 2013, 52, 11173−11184

^{17}O A_{iso} values. However, the averaged values do not differ significantly from the corresponding A_{iso} values obtained for the equilibrium geometry and remain very close to the experimental ones. These results suggest that ^{17}O HFCCs of coordinated water molecules in Mn^{2+} complexes can be estimated from the corresponding equilibrium geometries, most likely because of an approximately linear dependence of A_{iso} around the equilibrium configuration with respect to both the Mn−O_w distance and the Mn−O−H−H dihedral.

The ^{1}H HFCCs (Figure 7) calculated for each of the 100 snapshots extracted from the trajectory calculations correlate reasonably well with the corresponding ^{17}O A_{iso} values, which indicates that both ^{1}H and ^{17}O HFCCs are affected in a similar way by the Mn−O_w distances and large Mn−O−H−H dihedral angles. In line with our previous work, ^{17}O A_{iso} values are negative, while ^{1}H A_{iso} values are positive. However, these different signs correspond to positive spin densities at the point nucleus of both ^{17}O and ^{1}H, due to the different sign of the magnetic moment of these nuclei.

Calculation of ^{17}O and ^{1}H HFCCs in Related Systems. Isotropic ^{17}O and ^{1}H HFCCs in the $[Mn(CyDTA)(H_2O)]^{2-}\cdot 4H_2O$, $[Mn(1,4\text{-}DO2A)(H_2O)]\cdot 4H_2O$, $[Mn(L1)(H_2O)]\cdot 4H_2O$, $[Mn(L2)(H_2O)]^{+}\cdot 4H_2O$, and $[Mn(L3)(H_2O)_2]^{2+}\cdot 8H_2O$ systems (Scheme 1) were calculated in aqueous solution by using the same computational approach used for EDTA and MeNO2A complexes. The computed values are compared with the experimental ones in Table 3. These calculations were performed on the equilibrium geometries, and therefore dynamic effects were neglected. Our calculations provide A_{iso} values in general good agreement with the available experimental data, with deviations lower than 1.5% for the complexes of 1,4-DO2A, L1, and L2. The agreement with the experiment is however poorer in the case of the complex of L3, but the reasons for this discrepancy are still unclear. Taking together the data shown in Tables 1, 2, and 3, we conclude that the ^{17}O A_{iso} values fall within a relatively narrow range, typically −6.4 ± 0.9 MHz, which corresponds to $A_O/\hbar$ values of (40 ± 6) × 10^6 rad·s^{-1}. On the other hand, the calculated ^{1}H A_{iso} values are spread over a wider range (0.27−0.88 MHz), with an average value of 0.57 MHz.

Table 3. Calculated ^{17}O and ^{1}H Hyperfine Coupling Constants (A_{iso}, MHz) for the $[Mn(L)(H_2O)_q]^{n\pm}\cdot xH_2O$ Systems (L = CyDTA, 1,4-DO2A, L1, L2, or L3)

			^{17}O		
ligand	q	x	calcd	expt	$^{1}H^{a}$ calcd
CyDTA	1	4	−6.047		0.305(78)
1,4-DO2A	1	4	−6.773	−6.84[b]	0.267(18)
L1	1	4	−6.448	−6.35[c]	0.527(169)
L2	1	4	−5.876	−5.83[c]	0.876(95)
L3	2	8	−8.754	−6.14[d]	0.814(196)

[a]Averaged values are provided with standard deviations within parentheses. [b]Reference 10. [c]Reference 9. [d]Reference 15.

Spin Density Distributions. The spin density distribution in a given paramagnetic molecule denotes the difference between the contributions due to electrons with majority spin (α) and minority spin (β), which is the result of two effects: spin-delocalization, which results from the transmission of spin density through the bonds toward the observed nucleus, and spin-polarization, which is the result of an effective attraction of unpaired electrons to the nearby ones of the same spin.[49] For a given metal center with occupied α and unoccupied β orbitals, spin-delocalization can be identified either with metal to ligand α spin density donation or by donation of β spin density from the ligands to the metal center.[50] Both mechanisms create an excess of α spin density at the ligand nuclei, and therefore spin-delocalization gives always a positive contribution to the spin density, in contrast to spin-polarization, which can lead to positive or negative contributions. A characteristic pattern pointing to a spin-polarization effect is the presence of alternate spin density signs along the pathway of the bonded atoms radiating out from the paramagnetic atom.[51] This is for instance the case for Gd^{3+} complexes, in which the spin density is negative at the ^{17}O nucleus of coordinated water molecules and positive at their ^{1}H nuclei. Similar alternate spin density signs were also observed on the carbon nuclei of organic ligands coordinated to Gd^{3+}.[52]

In all geometric configurations obtained from the snapshots, the spin density at the position of the oxygen nucleus is positive, in accord with the spin delocalization mechanism (Figure 8). The spin density has a positive sign at both the ^{17}O and ^{1}H nuclei of the coordinated water molecule, indicating that the ^{1}H A_{iso} values are also dominated by the spin delocalization mechanism. The amount of spin delocalization is expected to increase with the covalent character of the metal−ligand bonds, and therefore it is not surprising that spin delocalization effects dominate the ^{17}O and ^{1}H HFCCs of Mn^{2+} complexes, while spin polarization is responsible for the observed A_{iso} values in Gd^{3+} complexes due to the limited radial extension of the metal 4f orbitals.

A close inspection of the contour spin density map obtained for $[Mn(MeNO2A)(H_2O)]\cdot 4H_2O$ shows that the spin density becomes negative at a certain point along the Mn−O axis. The molecular orbitals that host the unpaired electrons (SOMOs) in Mn^{2+} complexes should possess a major contribution from the metal d orbitals but are expected to mix with atomic orbitals of the ligands, particularly from the donor atoms. If spin delocalization is to dominate the spin density distribution, a distribution of positive spin density throughout the molecule determined by the composition of the SOMOs is expected to occur. The negative spin density observed along the Mn−O_{water} bond corresponds to a node of the SOMO (Figure 8) and can be therefore attributed to a weak spin-polarization effect that changes the sign of the spin density.

The effect of the Mn−O_w distance on the calculated ^{17}O A_{iso} values can be attributed to a rapid decay of the spin-delocalization effect upon increasing the distance between the metal ion and the oxygen atom of the coordinated water molecule. It must be borne in mind that the ^{17}O A_{iso} values result from the hyperfine coupling of the electronic and nuclear spins and therefore reflect only unpaired spin density at the ns orbitals, which do not have a node at the nuclear position. Thus, the following explanation can be given to the effect of the Mn−O−H−H dihedral angle on the calculated ^{17}O A_{iso} values: A dihedral angle of about 90° would imply that the water molecule uses a lone-pair placed on a p orbital to bind to the metal ion. As the dihedral angle increases, the s character of this lone pair is increasing as well, thereby increasing the probability of the unpaired spin density to sit just on the nucleus.

■ CONCLUSIONS

In this contribution, we have reported an easy access to the TACN-based ligand MeNO2A, which contains a methyl group and two acetate pendant functions attached to the nitrogen

dx.doi.org/10.1021/ic4014366 | Inorg. Chem. 2013, 52, 11173−11184

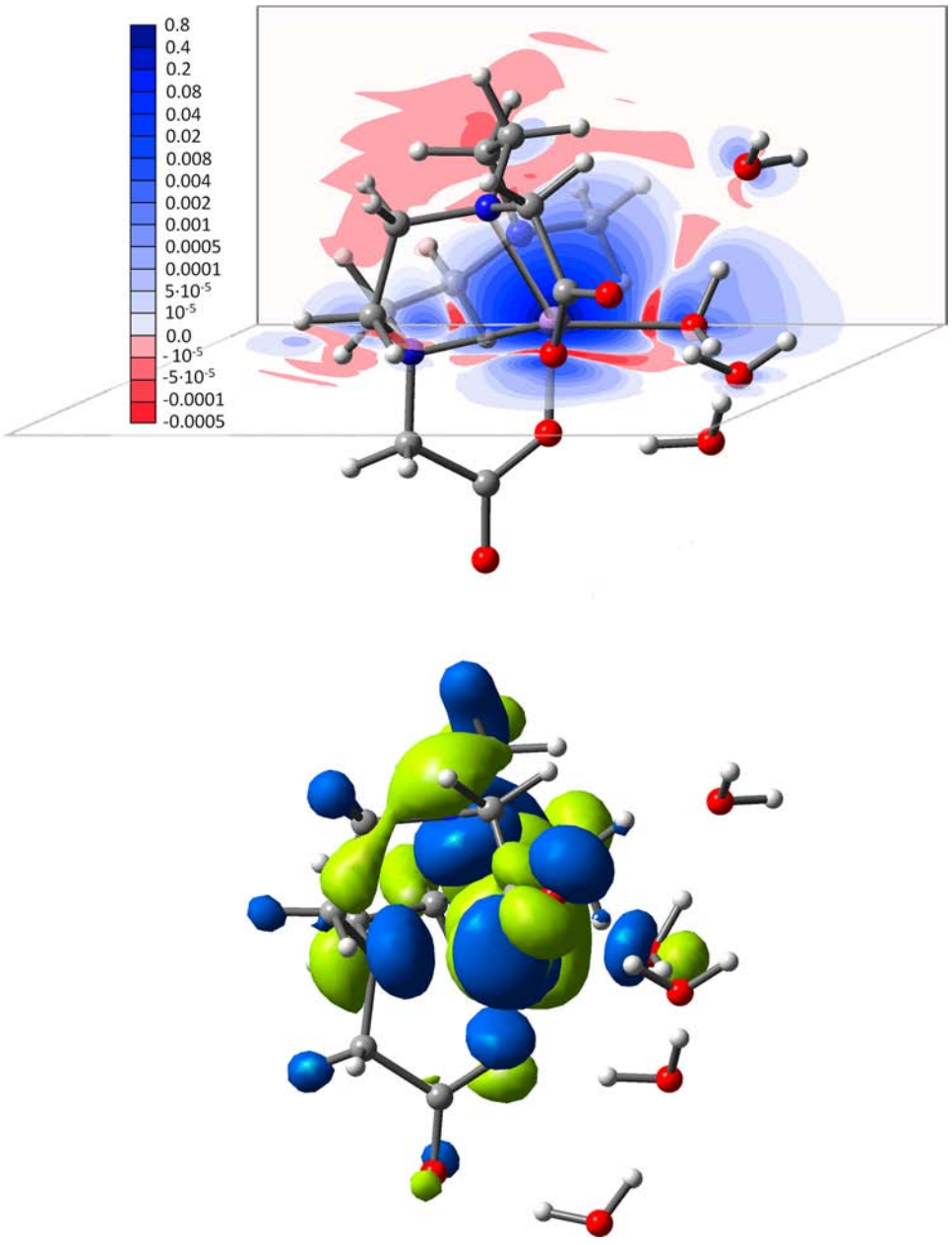

Figure 8. (top) Spin density map of the $[Mn(MeNO2A)(H_2O)]\cdot 4H_2O$ system (calculated at the TPSSh/TZVP/EPR-III, in au^{-3}) on the two planes defined by the Mn^{2+} ion, the oxygen atom of the coordinated water molecule, and its hydrogen atoms. (bottom) Surface plot of the highest SOMO calculated for $[Mn(MeNO2A)(H_2O)]\cdot 4H_2O$ at the same computational level.

atoms of the macrocycle. We have subsequently performed a ^1H and ^{17}O NMR relaxometric study of the $[Mn(MeNO2A)(H_2O)]$ complex as well as a theoretical analysis of the ^1H and ^{17}O HFCCs of the coordinated water molecule in this complex and related Mn^{2+} chelates relevant as MRI probes. Our DFT calculations show that the explicit inclusion of two to four second-sphere water molecules is crucial to obtain accurate $Mn-O_{water}$ distances and HFCCs. The use of a mixed cluster/continuum approach allows for a better description of the geometries and electronic structure of these systems at a reasonable computational cost, so that ADMP molecular dynamics simulations become feasible. Molecular dynamics simulations show that the ^1H and ^{17}O HFCCs on inner-sphere water molecules are very sensitive to the Mn−O distances and the orientation of the coordinated water molecule plane with respect to the Mn−O vector. However, the average HFCCs obtained from up to 100 snapshots extracted from trajectory calculations do not differ significantly from the corresponding A_{iso} values obtained for the equilibrium geometries and remain very close to the experimental ones. Thus, ^{17}O HFCCs of coordinated water molecules in Mn^{2+} complexes can be estimated to a good accuracy from the corresponding equilibrium geometries. Spin delocalization effects appear to dominate both the ^{17}O and ^1H A_{iso} values. With the notable exception of $[Mn(L3)(H_2O)_2]^{2+}$, the experimental and calculated ^{17}O A_{iso} values fall within a relatively narrow range (typically $A_{iso} = -6.4 \pm 0.9$ MHz or $A_O/\hbar = (40 \pm 6) \times 10^6$ rad·s^{-1}. Contrary to what was previously observed for $[Mn(H_2O)_6]^{2+}$,[53] the scalar contribution to relaxivity was found to be negligible for $[Mn(MeNO2A)(H_2O)]$.

dx.doi.org/10.1021/ic4014366 | *Inorg. Chem.* 2013, 52, 11173−11184

■ ASSOCIATED CONTENT

Supporting Information

^{1}H and ^{13}C NMR spectra of compounds **2**, **3**, **4**, and H_2MeNO2A, temperature dependence of r_{1p} for [Mn(MeNO2A)], equations used for the analysis of the NMRD and ^{17}O NMR data, and optimized Cartesian coordinates obtained with DFT calculations. This material is available free of charge via the Internet at http://pubs.acs.org.

■ AUTHOR INFORMATION

Corresponding Author

*E-mail address carlos.platas.iglesias@udc.es.

Notes

The authors declare no competing financial interest.

■ ACKNOWLEDGMENTS

The authors are indebted to Centro de Supercomputación de Galicia (CESGA) for providing the computer facilities. M.B. acknowledges Consorzio Interuniversitario di Ricerca in Chimica dei Metalli nei Sistemi Biologici (CIRCMSB). The authors also acknowledge the Ministère de l'Enseignement Supérieur et de la Recherche, the Centre National de la Recherche Scientifique, and the NMR facilities of the "Service Commun" of the University of Brest.

■ REFERENCES

(1) *The Chemistry of Contrast Agents in Medical Magnetic Resonance Imaging*, 2nd ed.; Merbach, A. E., Helm, L., Tóth, É., Eds.; Wiley: New York, 2013.

(2) (a) Caravan, P.; Ellinson, J. J.; McMurry, T. J.; Lauffer, R. B. *Chem. Rev.* **1999**, *99*, 2293−2352. (b) De Leon-Rodriguez, L. M.; Lubag, A. J. M.; Malloy, C. R.; Martinez, G. V.; Gillies, R. J.; Sherry, A. D. *Acc. Chem. Res.* **2009**, *42*, 948−957. (c) Chan, K. W.-Y.; Wong, W.-T. *Coord. Chem. Rev.* **2007**, *251*, 2428−2451. (d) Terreno, E.; Castelli, D. D.; Viale, A.; Aime, S. *Chem. Rev.* **2010**, *110*, 3019−3042.

(3) Drahos, B.; Lukes, I.; Toth, E. *Eur. J. Inorg. Chem.* **2012**, 1975−1986.

(4) Ducommun, Y.; Newman, K. E.; Merbach, A. E. *Inorg. Chem.* **1980**, *19*, 3696−3703.

(5) Maigut, J.; Meier, R.; Zahl, A.; van Eldik, R. *J. Am. Chem. Soc.* **2008**, *130*, 14556−14569.

(6) Cheng, S.; Abramova, L.; Saab, G.; Turabelidze, G.; Patel, P.; Arduino, M.; Hess, T.; Kallen, A.; Jhung, M. *JAMA, J. Am. Med. Assoc.* **2007**, *297*, 1542−1544.

(7) Aime, S.; Anelli, P. L.; Botta, M.; Brochetta, M.; Canton, S.; Fedeli, F.; Gianolio, E.; Terreno, E. *Biol. Inorg. Chem.* **2002**, *7*, 58−67.

(8) Rolla, G. A.; Tei, L.; Fekete, M.; Arena, F.; Gianolio, E.; Botta, M. *Bioorg. Med. Chem.* **2011**, *19*, 1115−1122.

(9) Drahos, B.; Kotek, J.; Cisarova, I.; Hermann, P.; Helm, L.; Lukes, I.; Toth, E. *Inorg. Chem.* **2011**, *50*, 12785−12801.

(10) Rolla, G. A.; Platas-Iglesias, C.; Botta, M.; Tei, L.; Helm, L. *Inorg. Chem.* **2013**, *52*, 3268−3279.

(11) Drahos, B.; Pniok, M.; Havlickova, J.; Kotek, J.; Cisarova, I.; Hermann, P.; Lukes, I.; Toth, E. *Dalton Trans.* **2011**, *40*, 10131−10146.

(12) Balogh, E.; He, Z.; Hsieh, W.; Liu, S.; Toth, E. *Inorg. Chem.* **2007**, *46*, 238−250.

(13) de Sa, A.; Bonnet, C. S.; Geraldes, C. F. G. C.; Toth, E.; Ferreira, P. M. T.; Andre, J. P. *Dalton Trans.* **2013**, *43*, 4522−4532.

(14) Tei, L.; Gugliotta, G.; Fekete, M.; Kalman, F. K.; Botta, M. *Dalton Trans.* **2011**, *40*, 2025−2032.

(15) Drahos, B.; Kotek, J.; Hermann, P.; Lukes, I.; Toth, E. *Inorg. Chem.* **2010**, *49*, 3224−3238.

(16) (a) Solomon, I. *Phys. Rev.* **1955**, *99*, 559−565. (b) Solomon, I.; Bloembergen, N. *J. Chem. Phys.* **1956**, *25*, 261−266. (c) Bloembergen, N. *J. Chem. Phys.* **1957**, *27*, 572−573. (d) Bloembergen, N.; Morgan, L. O. *J. Chem. Phys.* **1961**, *34*, 842−850.

(17) Al Derzi, A. R.; Fau, S.; Bartlett, R. J. *J. Phys. Chem. A* **2003**, *107*, 6656−6667.

(18) Barone, V.; Cimino, P.; Pedone, A. *Magn. Reson. Chem.* **2010**, *48*, S11−S22.

(19) Saladino, A. C.; Larsen, S. C. *Catal. Today* **2005**, *105*, 122−133.

(20) (a) Yazyev, O. V.; Helm, L.; Malkin, V. G.; Malkina, O. L. *J. Phys. Chem. A* **2005**, *109*, 10997−11005. (b) Yazyev, O. V.; Helm, L. *J. Chem. Phys.* **2007**, *127*, No. 084506.

(21) Esteban-Gomez, D.; de Blas, A.; Rodriguez-Blas, T.; Helm, L.; Platas-Iglesias, C. *ChemPhysChem* **2012**, *13*, 3640−3650.

(22) (a) Roger, M.; Patinec, V.; Bourgeois, M.; Tripier, R.; Triki, S.; Handel, H. *Tetrahedron* **2012**, *68*, 5637−5643. (b) Chong, H.; Brechbiel, M. W. *Synth. Commun.* **2003**, *33*, 1147−1154. (c) Kovacs, Z.; Sherry, D. A. *Tetrahedron Lett.* **1995**, *36*, 9269−9272. (d) Kruper, J. W.; Rudolf, P. R.; Langhoff, C. A. *J. Org. Chem.* **1993**, *58*, 3869−3876. (e) Van Westrenen, J.; Sherry, D. A. *Bioconjugate Chem.* **1992**, *3*, 524−532.

(23) (a) Gasser, G.; Tjioe, L.; Graham, B.; Belousoff, M. J.; Juran, S.; Walther, M.; Künstler, J. U.; Bergmann, R.; Stephan, H.; Spiccia, L. *Bioconjugate Chem.* **2008**, *19*, 719−730. (b) Stavila, V.; Allali, M.; Canaple, L.; Storzt, Y.; Franc, C.; Maurin, P.; Beuf, O.; Dufay, O.; Samarut, J.; Janier, M.; Hasserodt, J. *New J. Chem.* **2008**, *32*, 428−435. (c) Roger, M.; Lima, L. M. P.; Frindel, M.; Platas-Iglesias, C.; Gestin, J. F.; Delgado, R.; Patinec, V.; Tripier, R. *Inorg. Chem.* **2013**, *52*, 5246−5259.

(24) Neese, F. *Coord. Chem. Rev.* **2009**, *253*, 526−563.

(25) (a) Zimmerman, J. R.; Brittin, W. E. *J. Phys. Chem.* **1957**, *61*, 1328−1333. (b) Swift, T. J.; Connick, R. E. *J. Chem. Phys.* **1962**, *37*, 307−320. (c) Leigh, J. S., Jr. *J. Magn. Reson.* **1971**, *4*, 308−311. (d) McLaughlin, A. C.; Leigh, J. S., Jr. *J. Magn. Reson.* **1973**, *9*, 296−304.

(26) McLachlan, A. D. *Proc. R. Soc. London, Ser. A* **1964**, *280*, 271−288.

(27) Southwood-Jones, R. V.; Earl, W. L.; Newman, K. E.; Merbach, A. E. *J. Chem. Phys.* **1980**, *73*, 5909−5918.

(28) Frisch, M. J.; Trucks, G. W.; Schlegel, H. B.; Scuseria, G. E.; Robb, M. A.; Cheeseman, J. R.; Scalmani, G.; Barone, V.; Mennucci, B.; Petersson, G. A.; Nakatsuji, H.; Caricato, M.; Li, X.; Hratchian, H. P.; Izmaylov, A. F.; Bloino, J.; Zheng, G.; Sonnenberg, J. L.; Hada, M.; Ehara, M.; Toyota, K.; Fukuda, R.; Hasegawa, J.; Ishida, M.; Nakajima, T.; Honda, Y.; Kitao, O.; Nakai, H.; Vreven, T.; Montgomery, J. A., Jr.; Peralta, J. E.; Ogliaro, F.; Bearpark, M.; Heyd, J. J.; Brothers, E.; Kudin, K. N.; Staroverov, V. N.; Kobayashi, R.; Normand, J.; Raghavachari, K.; Rendell, A.; Burant, J. C.; Iyengar, S. S.; Tomasi, J.; Cossi, M.; Rega, N.; Millam, J. M.; Klene, M.; Knox, J. E.; Cross, J. B.; Bakken, V.; Adamo, C.; Jaramillo, J.; Gomperts, R.; Stratmann, R. E.; Yazyev, O.; Austin, A. J.; Cammi, R.; Pomelli, C.; Ochterski, J. W.; Martin, R. L.; Morokuma, K.; Zakrzewski, V. G.; Voth, G. A.; Salvador, P.; Dannenberg, J. J.; Dapprich, S.; Daniels, A. D.; Farkas, O.; Foresman, J. B.; Ortiz, J. V.; Cioslowski, J.; Fox, D. J. *Gaussian 09*, revision B.01; Gaussian, Inc.: Wallingford, CT, 2009.

(29) Becke, A. D. *J. Chem. Phys.* **1993**, *98*, 5648−5652.

(30) Lee, C.; Yang, W.; Parr, R. G. *Phys. Rev. B* **1988**, *37*, 785−789.

(31) Tao, J. M.; Perdew, J. P.; Staroverov, V. N.; Scuseria, G. E. *Phys. Rev. Lett.* **2003**, *91*, No. 146401.

(32) Schaefer, A.; Horn, H.; Ahlrichs, R. *J. Chem. Phys.* **1992**, *97*, 2571−2577.

(33) Stanton, J. F.; Gauss, J. *Adv. Chem. Phys.* **2003**, *125*, 101−146.

(34) Montoya, A.; Truong, T. N.; Sarofim, A. F. *J. Phys. Chem. A* **2000**, *124*, 6108−6110.

(35) Roca-Sabio, A.; Regueiro-Figueroa, M.; Esteban-Gomez, D.; de Blas, A.; Rodriguez-Blas, T.; Platas-Iglesias, C. *Comput. Theor. Chem.* **2012**, *999*, 93−104.

(36) Csonka, G. I.; Perdew, J. P.; Ruzsinszky, A. *J. Chem. Theory Comput.* **2010**, *6*, 3688−3703.

(37) Rydberg, P.; Olsen, L. *J. Phys. Chem. A* **2009**, *113*, 11949−11953.

(38) Orio, M.; Pantazis, D. A.; Neese, F. *Photosynth. Res.* **2009**, *102*, 443−453.
(39) Rega, N.; Cossi, M.; Barone, V. J. *J. Chem. Phys.* **1996**, *105*, 11060−11067.
(40) Schaefer, A.; Huber, C.; Ahlrichs, R. *J. Chem. Phys.* **1994**, *100*, 5829−5835.
(41) (a) Iyengar, S. S.; Schlegel, H. B.; Millam, J. M.; Voth, G. A.; G. Scuseria, E.; Frisch, M. J. *J. Chem. Phys.* **2001**, *115*, 10291−10302. (b) Schlegel, H. B.; Millam, J. M.; Iyengar, S. S.; Voth, G. A.; Scuseria, G. E.; Daniels, A. D.; Frisch, M. J. *J. Chem. Phys.* **2001**, *114*, 9758−9763. (c) Schlegel, H. B.; Iyengar, S. S.; Li, X.; Millam, J. M.; Voth, G. A.; Scuseria, G. E.; Frisch, M. J. *J. Chem. Phys.* **2002**, *117*, 8694−8704.
(42) Tomasi, J.; Mennucci, B.; Cammi, R. *Chem. Rev.* **2005**, *105*, 2999−3093.
(43) Ellis, D.; Farrugia, L. F.; Hickman, D. T.; Lovatt, P. A.; Peacock, R. D. *Chem. Commun.* **1996**, 1817−1818.
(44) Freed, J. H. *J. Chem. Phys.* **1978**, *68*, 4034−4037.
(45) Mills, R. *J. Phys. Chem.* **1973**, *77*, 685−688.
(46) Wang, X. F.; Gao, J.; Wang, J.; Zhang, Zh. H.; Wang, Y. F.; Chen, L. J.; Sun, W.; Zhang, X. D. *J. Struct. Chem.* **2008**, *49*, 724−731.
(47) (a) Pliego, J. R.; Riveros, J. M. *J. Phys. Chem. A* **2001**, *105*, 7241−7247. (b) Bryantsev, V. S.; Diallo, M. S.; Goddart, W. A., III *J. Phys. Chem. B* **2008**, *112*, 9709−9719. (c) Bryantsev, V. S.; Diallo, M. S.; Goddart, W. A., III *J. Phys. Chem. A* **2009**, *113*, 9559−9567.
(48) Iyengar, S. S.; Schlegel, H. B.; Voth, G. A. *J. Phys. Chem. A* **2003**, *107*, 7269−7277.
(49) Bertini, I.; Luchinat, C. *Coord. Chem. Rev.* **1996**, *150*, 29−75.
(50) (a) Aquino, F.; Pritchard, B.; Autschbach, J. *J. Chem. Theory Comput.* **2012**, *8*, 598−609. (b) Pritchard, B.; Autschbach, J. *Inorg. Chem.* **2012**, *51*, 8340−8351.
(51) Ruiz, E.; Cirera, J.; Alvarez, S. *Coord. Chem. Rev.* **2005**, *249*, 2649−2660.
(52) Lisowski, J.; Sessler, J. L.; Mody, T. D. *Inorg. Chem.* **1995**, *34*, 4336−4342.
(53) Bertini, I.; Briganti, F.; Xia, Z.; Luchinat, C. *J. Magn. Reson., Ser. A* **1993**, *101*, 198−201.